Construction and Building Materials 257 (2020) 119595

Contents lists available at ScienceDirect

Construction and Building Materials

journal homepage: www.elsevier.com/locate/conbuildmat

The importance of physical parameters for the penetration depth of impregnation products into cementitious materials: Modelling and experimental study

Janez Perko [a,*], Rafael Zarzuela [b], Inés Garcia-Lodeiro [c], María Teresa Blanco-Varela [c], Maria J. Mosquera [b], Timo Seemann [d], Li Yu [a]

[a] Belgian Nuclear Research Centre SCK•CEN, Boeretang 200, B-2400 Mol, Belgium
[b] University of Cádiz, Campus Puerto Real, 11510 Cádiz, Spain
[c] Spanish National Research Council CSIC, Eduardo Torroja Institute, Serrano Galvache 4, 28033 Madrid, Spain
[d] University of Aachen, Institute for Clay & Interface Mineralogy, 52072 Aachen, Germany

HIGHLIGHTS

- Combined experimental and modelling analysis of sol penetration.
- The importance of sol parameters for penetration depth depends on material pore size distribution.
- Surface tension and gelation time are the most important parameters for penetration depth.

GRAPHICAL ABSTRACT

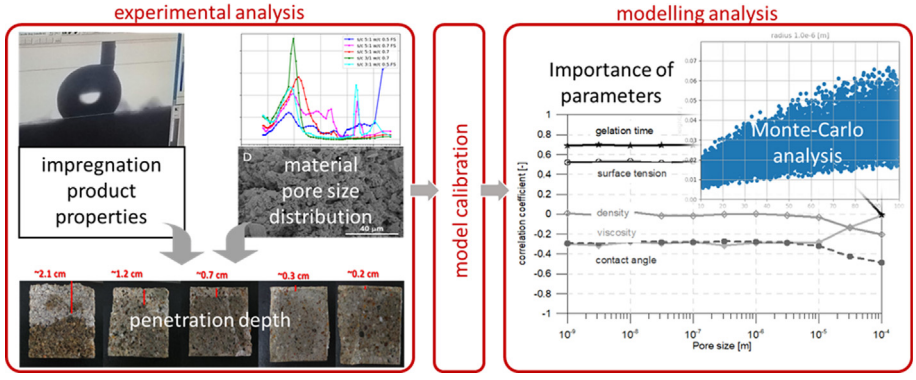

ARTICLE INFO

Article history:
Received 25 March 2020
Received in revised form 13 May 2020
Accepted 15 May 2020
Available online 25 May 2020

Keywords:
Penetration depth
Pore size distribution
Mortars
Impregnation products
Modelling analysis

ABSTRACT

The performance of impregnation treatments used for protection and remediation of porous building materials relies on sufficient penetration depth. The penetration of sol–gel impregnation products into partially saturated porous material is driven by capillary suction and depends on material properties, such as pore size distribution on one hand, and on the other hand on sol physical properties, viscosity, density, surface tension and contact angle, along with the time in which the sol gels. In this work we analyse, by the way of modelling and experiments, the penetration depth of a sol–gel impregnation product as the function of pore size distribution and sol properties. The main goal is to determine the importance of sol's physical properties for the penetration depth for a specific pore size, which will serve as a basis of the optimization of impregnation products to maximize their penetration depth. The model is first calibrated in terms of penetration depth and sol uptake by the experimental data obtained from mortar samples each with a specific pore-size distribution. The correlation between penetration depth and physical parameters is then established by the use of Monte-Carlo method. The results show that the most important parameters for the optimization are surface tension, whose influence increases for larger pores, and gelation time, which with decreasing importance for larger pores.

* Corresponding author at: Belgian Nuclear Research Centre SCK CEN Institute for Environment, Health and Safety Boeretang 200, B-2400 Mol Belgium.
E-mail address: janez.perko@sckcen.be (J. Perko).

https://doi.org/10.1016/j.conbuildmat.2020.119595
0950-0618/

1. Introduction

One of the pertinent concerns in the fields of civil engineering and cultural heritage preservation refers to the durability of building materials, which are exposed to increasingly aggressive environments due to factors such as pollution and climate change [1]. More specifically, cementitious materials (concrete, cement mortars...), which became the most employed since the late XIX century, are susceptible to a wide variety of decay processes [2,3], including but not limited to: damages by freeze–thaw cycles or thermal expansion, erosion by wind, ingress of chlorides from marine aerosols that causes salt efflorescence and rebar corrosion, calcium leaching by acid rain, carbonation by reaction with CO_2, etc. Continuous exposure to such conditions leads to cumulative damages that might eventually cause structural failure if left unattended and, subsequently, require expensive and time-consuming refurbishment and repair actions, aside from needing a regular maintenance to avoid further damages.

Due to the inherent costs and complexity of repair and maintenance works, there has been a growing interest in the development of preventive strategies to mitigate the effect of environmental agents [4,5]. For older buildings an appropriate route is the use conservation treatments that can be applied in situ on the building surface to increase its compaction and mechanical performance, which can be divided into coatings and impregnation treatments, according to EN 1504-2:2005 standard.

Among impregnation treatments, those based on alkoxysilanes (e.g. tetraethylorthosilicate) and their derivatives have been commonly used for the conservation of historical buildings [6] due to a series of advantages over other alternatives such as the ability to polymerize in situ by a sol–gel reaction with ambient moisture and formation of reaction products with a Si-O backbone that are stable and compatible with most building materials [31]. In addition to the aforementioned advantages, recent studies [7–9], show that alkoxysilanes may have a higher chemical compatibility with cementitious materials due to their reactions with components of their matrix [33]. More specifically, the silanol groups resulting from the hydrolysis stage can react with the portlandite yielding C-S-H gel, the main phase responsible of the cement matrix engineering properties, or get incorporated into the silica chains of the already existing C-S-H.

The effectiveness and durability of impregnation products is closely related with their penetration depth, which depends not only on the substrate characteristics such as pore size distribution [10], but also on the physical properties of the products such as surface tension, density, viscosity and contact angle. Moreover, intrinsic properties of the alkoxysilane-based treatments are not constant, since they change as a function of time [11] due to gelation and evaporation phenomena. Hence, the optimal penetration depth for a specific pore structure depends on many parameters which are not *a priori* fixed and, subsequently, the initial composition of the sol plays a key role. Due to the difficulty of accounting for such a large number of tuneable physical parameters, most experimental optimization studies focused only on a handful of parameters, such as viscosity [12]. A comprehensive study on the effect of porosity, relative humidity and time on the penetration depth of silanes in concrete has been performed in [13]. More elaborate sensitivity analysis, however, is time-consuming and experimentally difficult to perform. For this reason the methodology presented here combines experimental work with numerical analysis to determine the most important optimization parameters and their ranges. With respect to numerical analysis, there are several possibilities to model two phase flows in order to determine the infiltration depth. One approach is to explicitly model liquid absorption in a given pore micro structure. Recently, several lattice Boltzmann models were developed which can provide an information on interface tracking [14,15,32]. These models accurately describe fluid penetration into a given pore structure, but they are computationally intensive for 3D simulations. Moreover, the pore size distribution of cementitious materials shows that large portion of pores contributing to transport are in the range between 50 and 100 nm. In order to assure representative elementary volume (REV) of a model or reasonable penetration depth analysis required for the purpose of this work, exceedingly large number of voxels would be required, which entails large computational efforts. Thus, large calculation times make such models nonviable for the optimization purposes. Other possibility is to use pore-network models [16], but also here the scale differences between nano-pores and few centimeters of penetration depth that needs to be calculated makes these models not applicable for the optimization. Moreover, throats are still modelled as an ideal tubes and Hagen-Poiseuille flow with parabolic velocity distribution is assumed. As shown in the present work, this assumption is not correct for time dependent problems with time dependent physical properties.

To alleviate the computational issues, an abstracted approach based on Young-Laplace equation for the particular case of a cylindrical geometry is used in this work. This solution is known as Washburn equation [17], which describes the capillary rise of a partially wetting fluid in a cylindrical column. The model is fast and well suited for the optimization purposes, but it is not applicable for time variable parameters in the simplified form of Washburn's equation. Hence, in this work we used a differential form of Washburn's equation [18], which is based on the momentum balance, and is applicable to time-dependent physical parameters. On the basis of this model we evaluated the importance of different sol parameters towards the penetration depth at a set of given material properties (i.e. pore size distribution). The model is calibrated based on five experimentally characterized mortar samples with specific properties and one reference sol. The validation of the model is done by another weathered sample and in this way check the validity of calibrated parameters. Monte-Carlo analysis is then performed on the calibrated sol for the plausible parameter ranges. For each pore size, several thousand runs are performed with a random combination of parameters within this parameter space. Based on these results the partial rank correlation coefficient is calculated for each parameter and for each pore size. The results indicate that the importance and the sensitivity of each parameter to the penetration depth varies for different pore sizes and, therefore, the sol physical properties required to achieve an optimal penetration depth may vary depending on the material properties. The conclusions of the analysis are supported by an example of the sol application at lower temperature. We showed that the penetration depth doubled when the sol was applied at −10 °C compared to the application at room temperature (20 °C).

2. Mortar and sol properties

2.1. Sample preparation

Five sets of mortar samples were prepared for the analysis. Prismatic OPC mortar specimens ($4 \times 4 \times 16$ cm^3) were prepared using CEM I 42.5R cement and CEN-compliant sand. The cement composition is given in Table 1

In order to obtain specimens with different porosities and pore size distribution, three compositional parameters were modified: (1) the water-to-cement (w/c) ratios, (2) the sand-to-cement (s/c) ratios and (3) the presence/absence of fine sand aggregates. In the latter case the fraction of sand with particle size lower than 0.5 mm was removed by sieving. Analyzed samples are distin-

Table 1
Chemical composition of Cem I 42.5 (% Oxides in weight) (XRF).

Oxides	**CaO**	**Al_2O_3**	**SiO_2**	**SO_3**	**MgO**	**Fe_2O_3**	**Na_2O**	**K_2O**
Wt %	62.98	5.63	18.72	3.05	0.87	2.68	0.04	0.85
Oxides	**TiO_2**	**SrO**	**Cr_2O3**	**Cl**	**ZnO**	**P_2O_5**	**LOI(1)**	
Wt %	0.23	0.051	0.00	0.02	0.028	0.05	2.31	

(1)Loss of ignition 1000 °C.

guished on the basis of w/c, s/c and fine sand fraction included or not (FS) and are shown in Table 2.

No demolding product was added, since it may affect the penetration of the sol. Instead, the mold surface was covered by an adhesive film. After demolding the curing process was performed according to the standard EN 196-1, where mortars are immersed in water at 21 °C during 28 days. Additional time in the oven (4 days at 40 °C) was carried out to remove the excess of water and to obtain constant weight before applying the product. Drying in the vacuum oven has been used because it allows to dry the samples faster and at lower temperatures than a conventional oven, thus avoiding thus avoiding alteration of sensitive phases (e.g. ettringite) or damages due to thermal stress.

2.2. Pore size distribution and characteristics

For all prepared samples the characterization has been performed using MIP (Mercury Intrusion Porosimetry) on a Micrometrics AutoPore IV 9500V1.09 pore sizer. Samples were soaked in isopropanol for two days and then dried in a desiccator prior to analysis. MIP provides information on the intrusion volume of mercury as a function of pressure. The resulting intrusion curve is transformed into an equivalent pore frequency or equivalent pore size distribution assuming a cylindrical pore geometry and a contact angle of mercury of 138°. Integration over all pore size frequencies results in the material's porosity and averaging provides information on a mean equivalent pore size. The results are given in Table 3.

As expected, increasing the sand/cement ratio leads to a higher porosity, from ~13% at 3/1 s/c to 15–16% at s/c 5/1 due to the lower amount of cement hydration products. The w/c ratio increases the porosity, as observed by comparing the samples s/c 5/1 w/c 0.7 FS (16.73%) and s/c 5/1 w/c 0.5 FS (16.47%). The small difference between those values can be explained by the poor workability of s/c 5/1 w/c 0.5 FS (water proportion was too low), which increases the porosity of the mortar. The presence of fine sand aggregate leads to a more packed structure, which is manifested by the lower porosity values of s/c 3/1 w/c 0.5 and 5/1 w/c 0.7 compared to s/c 3/1 w/c 0.5 FS and s/c 5/1 w/c 0.7 FS respectively.

The limitation of the mercury intrusion is that all pores are assumed to be equally accessible to the exterior mercury reservoir. This assumption can only be met if the pore structure is represented in the form of a bundle of capillaries or if pore connectivity is very high. In reality, however, pore network effects can be quite important resulting in the so-called ink-bottle phenomenon. In other words, smaller pores connecting larger pores with the reservoir can only be filled at a pressure higher than that required by actual dimensions of a larger pore [16]. However, our problem of sol penetration from the surface involves the same mechanism of penetration into porous material and same ink-bottle effect is observed by sol and so the MIP measurement is preferred method for pore-size distribution analysis.

Table 2
Mortar samples used for the analysis.

Sample name	w/c	s/c	Fine sand (FS)
s/c 3/1 w/c 0.5 FS	0.5	3/1	No
s/c/ 3/1 w/c 0.7	0.7	3/1	Yes
s/c 5/1 w/c 0.7	0.7	5/1	Yes
s/c 5/1 w/c 0.7 FS	0.7	5/1	No
s/c 5/1 w/c 0.5 FS	0.7	5/1	No

Table 3
Measured porosity and average pore size in the analysed samples.

Sample name	Porosity (%)	Average pore Ø (μm)
s/c 3/1 w/c 0.5 FS	13.74	0.0464
s/c 3/1 w/c 0.7	13.21	0.0380
s/c 5/1 w/c 0.7	14.90	0.0575
s/c 5/1 w/c 0.7 FS	16.73	0.0778
s/c 5/1 w/c 0.5 FS	16.47	0.1209

Regarding the pore size, the samples with fine sand fraction (s/c 3/1 w/c 0.7 and s/c 5/1 w/c 0.7) are characterized by a narrower mono-modal distribution and smaller average pore sizes, indicating that the larger pores are filled by the fine sand. The samples without the fine sand fraction, on the other hand, show a higher frequency of larger pores and higher dispersion, as seen by their multi-modal distributions and the wide peaks observed for s/c 5/1 w/c 0.5 FS and s/c 5/1 w/c 0.7 FS, where some distinct peaks are combined with less frequent pore sizes. This effect is illustrated by the SEM micrographs of s/c 5/1 w/c 0.7 and s/c 5/1 w/c 0.7 FS (Fig. 2C–D), where the latter shows a higher number of voids in the 1–10 μm size range.

With respect to the influence of s/c ratios, it was observed that the samples with 5/1 show a higher frequency of larger pore sizes than with 3/1, because of higher amount of OPC hydration products in the latter. The effect of the w/c ratio to pore size distribution is more complex. While higher w/c ratios in general increase the pore size, the amount of water in 5/1 w/c 0.5 FS was too small to properly mix the components, leading to larger voids in the structure as shown in Fig. 2.

In Fig. 2 we can also observe two distinct narrow peaks at the pore size around 25 μm for two cases, s/c 5/1 w/c 0.7 FS and s/c 3/1 w/c 0.5 FS, respectively. These peaks, as deducted from the analysis in section 3.2, are not a consequence of a large number of uniform pores of this particular size, but instead represent prolonged microcracks. The presence of such cracks was experimentally confirmed by the SEM micrographs from the cross-sections (Fig. 1A).

While the pore size distribution provides the information on accessible porosity and the frequency distribution of pores of a certain size, there is no information on pore characteristics in terms of it length. This information is crucial to determine the uptake of impregnation products and determines the number of pores of a certain size.

On the basis of SEM analysis [19] it has been estimated that the length of pores of μm size is 3–7 times their diameter. Furthermore, it has been observed that the ratio is smaller at smaller pores (e.g. nano-pores are less prolonged than micro-pores). Hence, we assume that the ratio of pore length/pore diameter increases with the pore diameter. We call this length a characteristic length h_{char} as a function of pore size.

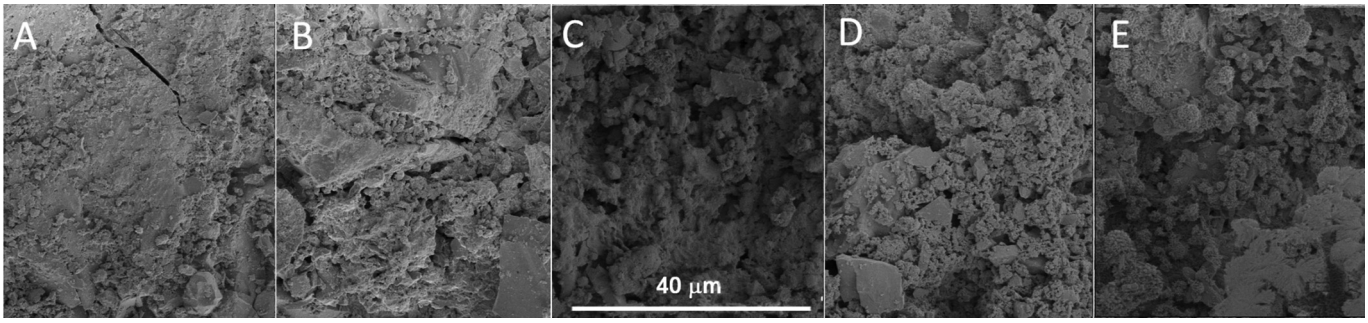

Fig. 1. Cross-section SEM micrographs of the different mortars. (A) 3/1 w/c 0.5 FS, (B) 3/1 w/c 0.7, (C) 5/1 w/c 0.7, (D) 5/1 w/c 0.7 FS, (E) 5/1 w/c 0.5 FS.

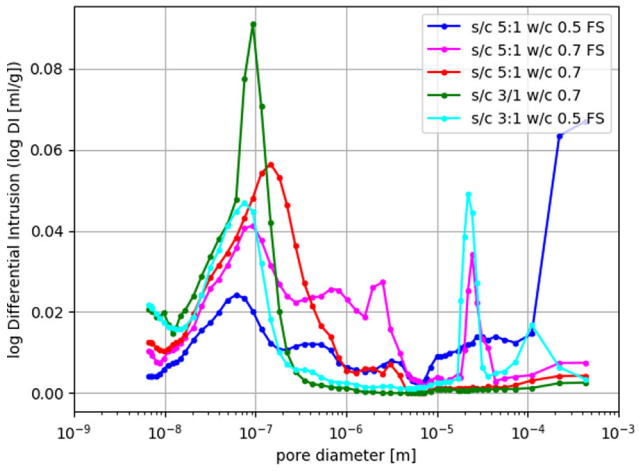

Fig. 2. Pore size distributions of examined samples.

2.3. Sol parameters

The impregnation product employed in this work is synthetized via a sol–gel route [20]. It consists of a low-viscosity sols that can be easily applied to cement-based buildings and polymerize in-situ, forming a silica xerogel and/or C-S-H gel in the presence of cement components. The starting sols contained the following components:

(i) An oligomeric silica precursor: admixture of monomeric and oligomeric ethoxysilanes;
(ii) n-octylamine, which acts as a catalyst of the sol–gel process and as a surfactant;
(iii) De-ionized water, which acts as a reagent and allows the formation of inverse micelles in the reaction media;

Resulting sol physical properties are characterized by four relevant parameters, contact angle θ [°], viscosity μ [mPa•s], surface tension σ [mN/m] and density ρ [kg/m^3]. All these parameter values are time dependent due to the gelation process or evaporation of ethanol (gelation byproduct) from the sol.

Viscosity of the sol was measured by using a concentric cylinder viscometer (DV-II + with UL/Y adapter, Brookfield). The surface tension of the sol and its contact angles with an OPC mortar were recorded employing a commercial video-based, software-controlled contact angle analyzer (OCA15plus, Dataphysics Instruments with SCA20/22 software). Surface tension was determined by the pendant drop method, whereas the contact angle was measured by the sessile drop method.

For the reference sol, the contact angle and viscosity have been measured with time. On the other hand, the surface tension and density are measured at the initial state only, as preliminary measurements showed no significant changes. The experimental measurement of accurate contact angle values is difficult because of two main factors: (1) the droplet is quickly absorbed inside the material due to its porosity, thus the measurement was performed at the initial contact time (2) the mortar surface is chemically heterogeneous and has a high roughness, which will affect the measurement as predicted by the Wenzel wetting model [21]. Because of this, the data may still be subject to a significant error, and this value will be calibrated by the numerical model. Measured values are given in Table 4.

For the purpose of the use in the numerical model, the tabulated values are parametrized and fitted to a function. The viscosity increases almost linearly in three consecutive steps as shown in Fig. 3. For the approximation we can use a simple linear relation $\mu = a + b(t - t_0)$ for the three consecutive periods as given in Table 5. The first step (<3h) corresponds the hydrolysis and formation of low molecular weight silica nuclei. Afterwards, the nuclei start to grow and viscosity increases slightly faster. After 13 h, the sharp viscosity increase indicates the condensation stage of the sol–gel process, which leads to a fast increase of the SiO_2 chains molecular weight. Between 16 and 17 h, the viscosity values suddenly grow as the sol becomes a solid.

The result of the fitting procedure is shown in Fig. 3(left). Generally, contact angle and surface tension are not directly related to viscosity and separate experiments are required. Experimental results show that the contact angle progressively increases with time (lower wettability), until reaching stable values after 5 h. The observed trend suggests that the contact angle mainly depends on the hydrolysis stage of the sol–gel process, where the ethoxy-groups in the sol evolve towards silanols. In literature the contact angle for water on concrete powders is reported to be approximately 70° [34]. In our experiments, however, the contact angle remains at around 30° as observed in Fig. 3(right).

The contact angle has been fitted by the following relation

Table 4
Experimentally determined time variable contact angle and viscosity.

Time [h]	Contact angle [deg]	Viscosity [mPa·s]
0	15.22	4.53
1	22.93	4.92
2	26.85	5.15
3	27.17	5.39
4	30.77	6.21
5	31.87	6.52
7	32.73	7.11
12	32.32	9.25
13	33.44	9.49
14	32.71	11.2
15	31.95	13.1
16	32.16	14.6

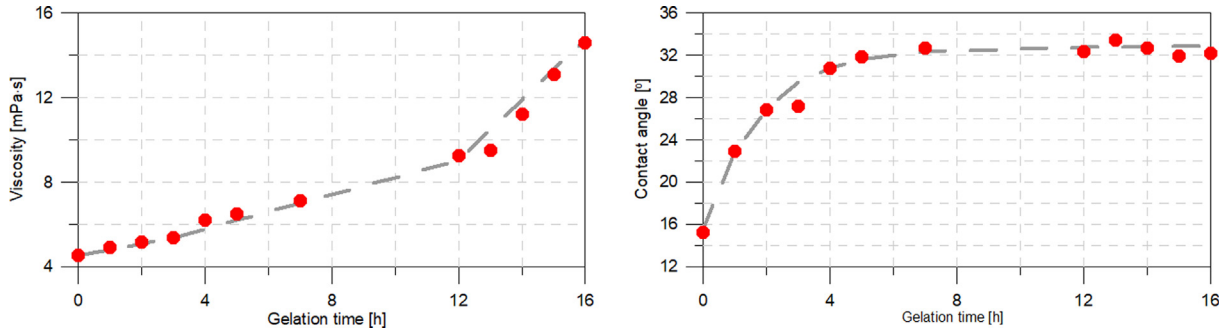

Fig. 3. (left) Viscosity evolution versus time and (right) Contact angle versus time. Experimental data (dots), approximated data (dashed line).

Table 5
Fit parameters for the experimentally determined time variable viscosity.

Time [h]	a	b	t0
t < 3	4.53	0.281	0
3 < t < 13	3•4.53	0.384	3
13 < t < 16	3•4.53 + 12•0.384	1.723	12

$$\theta(t) = \theta_0 + 0.01277 \cdot t - 17.133 \cdot e^{-0.55\,t} \; (t \leq 16h) \quad (1)$$

Where $\theta_0 = 32.63^{\circ}$.

Both, contact angle and viscosity experience a sudden change in their physical properties when gelation takes place and this happens between 16 h and 17 h. Surface tension was measured at the initial state and the value was fixed at 21.2 mN/m. Time dependent measurements at longer times were not performed due to experimental difficulties. Namely, the measurement method used to determine surface tension (pendant drop) requires knowing drop volume, which is difficult to control when the gelation starts.

2.4. Penetration depth and uptake

Prior to the application of the impregnation product, the mortar samples were cut into 4 × 4 × 4 cm cubes and the surfaces selected for the application were polished with P180 grit sandpaper. Afterward, the samples were cleaned with a pressurized air gun (2 bars), immersed in an ultrasound bath with deionized water for 15 min and dried at 40 °C. Finally, they were conditioned at atmospheric conditions (20 °C, 40% RH) for 4 days.

The impregnation product was applied by brushing on a single face until apparent saturation. Between each application, the sample was left 5 min to absorb the sol. The uptake was determined by the weight difference before and after the treatment. The treated samples cured for 24 h at atmospheric conditions (20 °C, 40% RH).

The penetration depth was experimentally determined via acid etching. For this purpose, the mortar cubes were cut in half and the cross-section was dipped in a 0.1 M HNO_3 solution for 15 s and afterwards cleaned with de-ionized water. As shown in Fig. 4, the regions where the treatment is present are more resistant to the acid and, therefore, absorb less water than the damaged ones. For homogeneous materials, it is fairly straightforward to determine the penetration depth, but for degraded or fractured material the penetration depth can vary significantly. In the latter case, the penetration depth was estimated as the average value between ten evenly spaced measurement points for each sample.

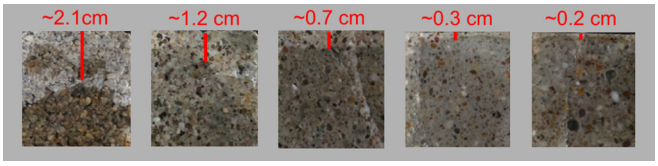

Fig. 4. Representative images of the mortar samples after acid etching and experimentally determined average penetration depths. Samples from left to right are: s/c 5/1 w/c 0.5 FS, s/c 5/1 w/c 0.7 FS, s/c 5/1 w/c 0.7, s/c 3/1 w/c 0.7, s/c 3/1 w/c 0.5 FS.

These measured values are reported in Table 6.

The highest degree of uptake and penetration depth is achieved in sample with highest total porosity and with the higher average pore size diameter. The highest uptake and penetration depth in Table 6 is seen for sample s/c 5/1 w/c 0.5 FS where we identify the highest % of pore volume larger than >100 μm, while the lowest penetration depths are seen for the samples with higher contribution of pores with lower pore size diameter.

3. Modelling analysis of penetration depth

3.1. Modelling approach

As discussed in the introduction, the purpose of the applied model is to be able to quickly analyse required optimized properties for any given pore structure. From above experimental analysis it is clear that a majority of pores responsible for sol penetration are in the range below 100 nm while the penetration depth can be up to the order of centimetres. This type of problem cannot be applied neither in the form of pore-scale model, nor as pore network model due to the practical limitations. Hence, the process of infiltration of sols into porous structure by capillary suction forces is approached by the use of column wicking experiments where the penetration rate is measured in the dependence of the effective radius $r[m]$, surface tension $\sigma[\frac{N}{m}]$, contact angle θ and viscosity $\mu[Pa \cdot s]$. In fact, MIP analysis is based on the assumption that all pores are equally available, or in other words, that the pore structure are represented by a bundle of cylindrical pores, which is the same assumption as used for column wicking experiments. The basic Washburn equation [20] is not sufficient for our purpose, because fluid properties are time dependent as described in Section 2.3. The equation needs to be rewritten in the differential form, where the momentum balance in Eq. (2) can be written as a sum of pressure resulting in the increase or decrease of the capillary rise of a given fluid with a contact to a given solid. The driving force is the Laplace pressure which is opposed by the hydrostatic pressure, the viscous pressure loss given by a Hagen-Poiseuille equation and the resistance due to inertial contributions [23] as given in Eq. (2). The hydrostatic pressure can have different sign depending on the orientation. In our case the hydrostatic pressure opposes suction forces, because the penetration depth is experimentally measured by wicking experiment.

$$\rho \frac{d(hv)}{dt} = \frac{2\sigma \cos\theta}{r} - \rho g h - \frac{8\mu h}{r^2}\frac{dh}{dt} \quad (2)$$

Table 6
Experimentally determined values of sol uptake and the penetration depth.

Sample	Porosity [%]	Average pore size [μm]	Uptake [g/m^2]	Penetration depth [mm]
s/c 3/1 w/c 0.5 FS	13.7	0.05	369	2
s/c 3/1 w/c 0.7	13.2	0.04	544	3
s/c 5/1 w/c 0.7	14.9	0.06	813	7
s/c 5/1 w/c 0.7 FS	16.7	0.08	1106	12
s/c 5/1 w/c 0.5 FS	16.5	0.12	1581	21

Given that in cement/mortar material we deal with small radii, velocities and consequently inertial forces are small and the left-hand side of Eq. (2) can be neglected. The resulting differential equation relating capillary rise as a function of time and other physical fluid-parameters is consequently defined as

$$\frac{dh}{dt} = \frac{2\sigma r \cos\theta}{8\mu h} - \frac{\rho g r^2}{8\mu} (\text{for } h > 0) \tag{3}$$

If the fluid contains charged ions, an electric field develops along the length of fluid. This results in a streaming potential which induces electroosmotic flow [18] acting as additional counter force towards capillary suction. This phenomenon is added as an additional term in the momentum balance (Eq. (2) and Eq. (3)) and defined as a function of the permittivity in vacuum ε_0, the relative dielectric constant of the fluid ε, the zeta potential ζ and the streaming potential U_{str} resulting in Eq. (5).

$$\frac{dh}{dt} = \frac{2\sigma r \cos\theta}{8\mu h} - \frac{\rho g r^2}{8\mu} - \frac{\varepsilon\varepsilon_0\zeta U_{str}}{\mu h} (\text{for } h > 0) \tag{4}$$

The last term in Eq. (4) is only significant when the other terms are small, which is valid for small pores. These pores contribute very little to the penetration depth and so this term is excluded from further analysis. Moreover, uncertainties regarding the dielectric properties and zeta potential are relatively large and the sol is unlikely to contain a large amount of charged ions because it is expected to have a low dissociation constants and because Ca^{2+} ions leached from the substrate will not reach high concentrations. The differential Eq. (4) is solved by a simple explicit finite difference solver.

$$h_{new} = h_{old} + \Delta t \left(\frac{2\sigma(t) r \cos\theta(t) - \rho g h_{old} r^2}{8\mu(t) h_{old}} \right) (\text{for } h_{old} > 0) \tag{5}$$

The initial condition for this system should be set to a small value otherwise the solution at the initial time is singular. The increments are initially large which requires small initial time steps to assure the convergence of the results. This is even more important for larger pores. We chose the initial time step arbitrarily as $\Delta t_{init} = 10^{-15}[s]$. This time step is multiplied by an increment t_{inc} each iteration until we reach the selected upper limit. t_{inc} is defined as $t_{inc} = 1 + 2 \cdot 10^{-10-log_{10} r}$. For our simulations we used 1000 s as the maximum time-step.

3.2. Model calibration

The model described by Eq. (5) runs across a whole spectra of pore sizes until the time of gelation is achieved. For each pore size a specific infiltration depth is calculated. The theoretical curve, which denotes the relation between the penetration depth based on the input parameters given in Section 2.3 and the pore size distribution is shown in Fig. 5.

The shape and magnitude of the penetration depth depends on the sol's physical properties. Fig. 5 indicates that the maximum infiltration height should be around 45 cm at pore size around 10 μm. However, experiments show much lower penetration depth (20 times lower). Obviously the idealized system described by Washburn's equation does not confirm experimentally measured values.

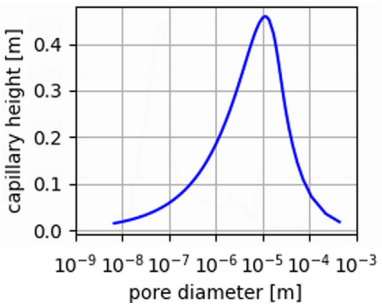

Fig. 5. Theoretically calculated capillary height for different pore sizes.

It needs to be noted here, that the experimentally determined penetration depth is an approximate value. Where the penetration depth is determined by a well-defined imbibition front, the values are easily measurable. However, in many cases capillary fingering along preferential pathways, possibly arising from micro cracks, are visible. In this case the penetration depth is visually approximated by putting more emphasis on the general penetration depth than on the discrete fingerings. When calculating the penetration depth computationally, this behavior is captured by using a generalized or power mean with an exponent of 0.5 as defined in in Eq. (6).

$$h_{penetration} = \left(\frac{\sum_i \left(V_i \cdot \sqrt{h_i} \right)}{\sum_i V_i} \right)^2 \tag{6}$$

Under the assumption that the pore is tube-shaped, the volume of absorbed sol can be calculated as

$$V_{sol} = \pi \sum_i N_i \cdot r_i^2 \cdot h_i \tag{7}$$

Where h_i is calculated from Eq. (7) and index i denotes the pore size class. The number of pores N_i is calculated from Eq. (9) with the volume of mercury ∇V_i intruded into pores of size r_i during the mercury intrusion porosimetry (MIP) and the total volume of pores V_{pi} of this size.

$$N_i = \nabla V_i / V_{pi} \tag{8}$$

The volume increment of mercury ∇V_i is derived from the pore-size distribution (log DI in Fig. 2) for each pore size as

$$\nabla V_i = \log DI \cdot (\log_{10} r_i - \log_{10} r_{i-1}) \tag{9}$$

Where r_i and r_{i-1} are two consecutive pore radii from PSD measurements. Taking forward our assumption that the length of a filled pore is related to the characteristic length and its radius we can determine the volume of one pore at each pore size. Hence the volume of one pore is

$$V_{pi} = \frac{h_{char}}{2r_i} \pi r_i^3 = \frac{h_{char}}{2} \pi r_i^2 \tag{10}$$

The characteristic length h_{char} is obtained by fitting as described below.

The model presented above has to be calibrated so that it corresponds to the measured penetration depth and sol uptake.

By comparison of the experimental data in Table 6 and the theoretically obtained penetration depths in Fig. 5 corresponding to a specific pore size distribution in Fig. 2 one can observe large differences between the experimental results and theoretical values. Clearly, the viscous pressure loss in cement pores is much larger than theoretically calculated. This is caused by different reasons, most likely due to the large surface roughness of the pores, which effectuates the parabolic flow assumed in Hagen-Poiseuille flow. The irregular shape of the pores in the real system is also a significant contribution. Additional pressure drop can be expressed as a multiplication factor λ to viscosity and Eq. (5) gets the form of Eq. (11)

$$h_{new} = h_{old} + \Delta t\left(\frac{2\sigma(t)r\cos\theta(t) - \rho g h_{old} r^2}{\lambda\mu(t)h_{old}}\right)(\text{for } h_{old} > 0) \qquad (11)$$

As explained above, the measurement of the contact angle θ is quite uncertain, because of the capillary suction forces of the porous mortar surface. We assume that the contact angle evolution with time will follow the same trend as it is measured (Fig. 5), but the initial value may change. Hence also the parameter θ_0 in Eq. (1) is taken into account in the calibration process.

In order to calibrate the sol uptake in the model we need to define the characteristic length of the pores of different sizes. In our calibration process we decided to divide pore size classes according to their magnitude size, starting from pores of sizes (d = 2r) lower than 10^{-7} m, 10^{-7} m < d < 10^{-6} m, 10^{-6} m < d < 10^{-5} m, 10^{-5} m < d < 10^{-4} m and pores >10^{-4} m.

For the calibration we used least-squares fitting in Julia [22] under an MIT license which utilizes the Levenberg-Marquardt algorithm for non-linear fitting. The fitted value is composed out of two target quantities, penetration depth and a specific mass uptake. Because the ranges of the fitted values differ considerably, we divided the uptake by 10, and the composed fitted value is Uptake/10 [g/m^2] + Depth [mm]. The calibrated parameters based on this optimization process are given in Eq. (12)

$$\begin{aligned}
&d < 10^{-7}m && h_{char} = 6\ \mu m\\
&10^{-7} \le d < 10^{-6}m && h_{char} = 7\ \mu m\\
&10^{-6} \le d < 10^{-5}m && h_{char} = 11\ \mu m\\
&10^{-5} \le d < 10^{-4}m && h_{char} = 6000\mu m\\
&d \ge 10^{-4}m && h_{char} = 30\mu m\\
&\theta_0 = 42^{\circ}\\
&\lambda = 2040
\end{aligned} \qquad (12)$$

From these results we can see that the real viscous pressure loss is 255 times larger than the theoretically calculated. In principle the pressure loss can be different for different pore sizes, but since the agreement with the experiment is reasonable, further refinement has not been performed at this step.

3.3. Model validation

In order to test the calibrated values and the model we made another experiment on a carbonated s/c 3/1 w/c 0.5 sample. After the curing process, samples were aged in a CO_2 incubator chamber (2% CO2, 25 °C, R.H > 80%) during 8 months. Porosity after carbonation reduced from 11.3% to 7.3%. This reduction is not equal for all pore sizes. The relative frequency of pore size classes is given in Table 7.

Experimental results in Table 7 show that the most abundant pore sizes in the intact material are between 10 and 100 nm. At the carbonation process, these pores are blocked by carbonation by-products and their frequency decreases for 21.5%. Conversely, pores smaller than 10 nm become more frequent due to the decalcification of C-S-H. The frequency of pores between 100 nm and 1 μm, increases for 10%. There is also a larger contribution of large pores which are resulting from the carbonation shrinkage (i.e. decrease of the smaller pores contribution).

Uptake and penetration depth for the carbonated sample are included in Fig. 6.

Table 7
Relative frequency of pore size classes.

Pore size class [μm]	Frequency intact [%]	Frequency carbonated [%]
>100	2.5	9.1
100–10	2.5	2.0
10–1	10.9	2.7
1–0.1	29.1	39.2
0.1–0.01	49.2	27.7
<0.01	5.9	19.3

3.4. Modelling results

Penetration depth and uptake of the calibrated model compared to the experimental values are shown in Fig. 6. Fig. 6 also indicates the results for the carbonated sample used for the model validation. In general, the results are in a good agreement with the experiments, especially regarding the uptake values. The penetration values, as previously explained, are subjected to a higher uncertainness due to the measurement method and the existence of preferential paths in the material. It is worth mentioning that the behavior on the carbonated mortar used for the validation closely fits to the theoretical values, in spite of its lower porosity which, *a priori*, would be expected to further decrease the uptake and penetration. This result highlights the importance of pore size distribution on the sol transport phenomena.

Based on the measured sol uptake we additionally estimated the number of pores of each size and consequently the amount of sol uptake at each pore size in order to receive information on which pores contribute the most to the uptake volume as described in Eqs. (8)–(10). Integration of these uptakes over all pore sizes provides the total uptake. The results of number of pores and sol uptake at different pore sizes are shown in Fig. 7. It can be seen that the number of small pores (e.g. gel pores) is in the order of magnitude of 10^{12} pores/cm^3. This is in line with the assumption given in [24] where the authors estimated the number of pores to similar values. Furthermore, we can observe that the number of pores decreases with the increase of pore sizes. The relation is close to linear from small sizes until a pore size of approximately 10 μm. We assume, based on SEM images, that the pores of 10 μm are in fact micro fractures. The number of these micro fractures is smaller compared to smaller pore sizes. Typically, their number is approximately 100–1000 per cm^3. Further we have larger number of pores >10 μm, which are probably part of the interfacial transition zone as described in [24,25].

The sol uptake is low at very small pore sizes, consequently leading to low contribution to penetration depths. The uptake rises until the pore sizes is around 50 nm where it reaches the maximum for materials with low amount of large pores, for example mortar with w/c = 0.7 and sand/cement = 3:1 with fine sand. Consequently, for such small pore sizes, the contribution to penetration depth is comparatively low. Materials with larger number of pores of sizes above 10 μm, have also larger uptake and higher penetration depth.

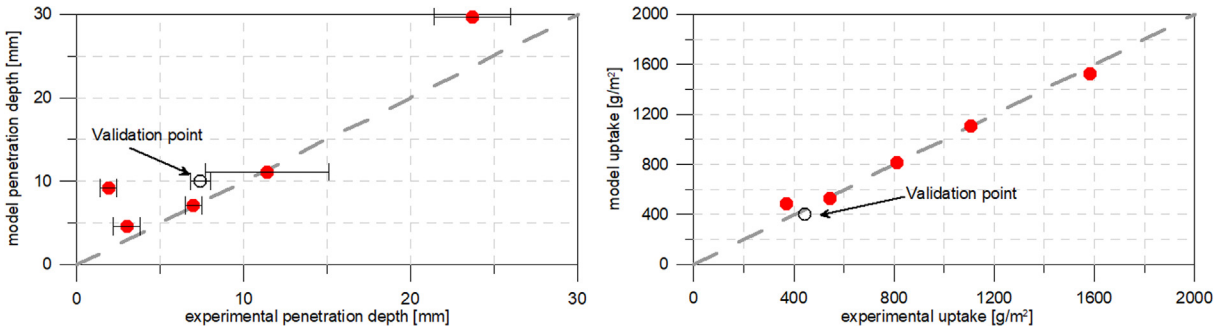

Fig. 6. Comparison between calibrated model and experimental results for (left) penetration depth including experimental sample standard deviation and (right) for uptake.

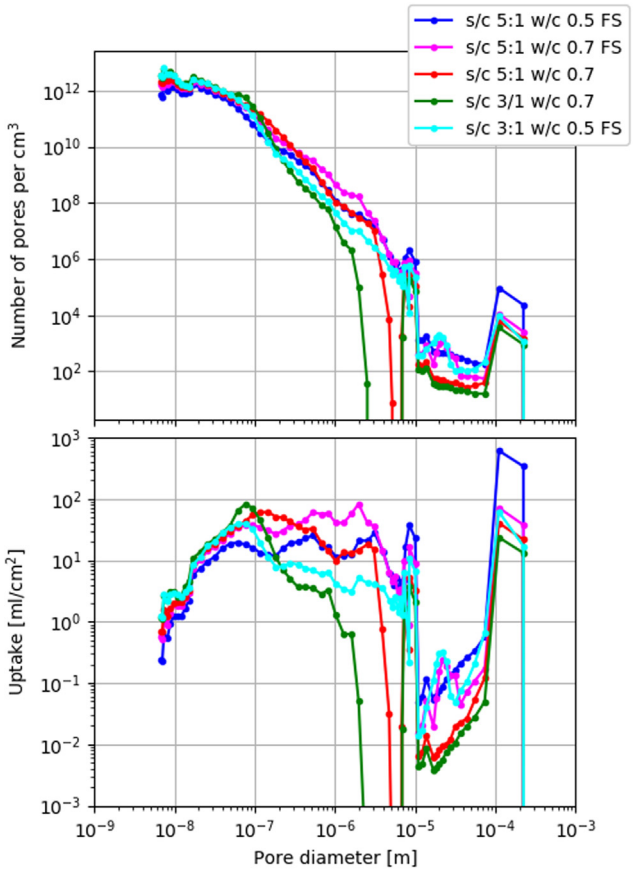

Fig. 7. Calculated number of pores (top) and total uptake of sol (bottom) at different pore sizes.

4. Sensitivity study

In order to be able to optimize the sol properties it is important to know which parameters are the most important for the penetration depth. Although the Eq. (3) is relatively simple, the result is not trivial since some input parameters are time dependent and non-linear. Therefore this study is performed by the use of global uncertainty and sensitivity analysis. Many techniques have been developed to address uncertainty and sensitivity analysis (see [27] and the references therein). In this work we use Monte-Carlo uncertainty analysis combined with the Partial Rank Correlation Coefficient (PRCC) sensitivity analysis index to determine the interactions between parameters. Monte Carlo (MC) methods are popular algorithms based on random sampling to obtain results from multiple model evaluations. MC uses random or pseudo-random numbers to sample from probability distributions of model inputs. PRCC is a suitable technique to quantify the relation between a given input and output of a model for nonlinear but monotonic relationships. The correlation provides a measure of the strength of a linear association between an input and an output. A correlation coefficient between input xj and output y is calculated as follows:

$$r_{x_i y} = \frac{Cov(x_j, y)}{\sqrt{Var(x_j)Var(y)}} \tag{13}$$

Values of $r_{x_i y}$ are between (-1 and 1), where −1 denotes perfect anti-correlation, 0 no correlation and 1 perfect correlation between parameter x_i and a result y. In our case x_j and y are ranked variables, which result in Spearman's coefficient. The calculations are performed for different pore sizes, starting from 10^{-9} m to 10^{-4} m. Parameter ranges used in the analysis are given in Table 8.

Gelation time is the time at which the sol becomes solid. Here we assume here that the gelation progresses in the same way (i.e. having the same shape), but with different kinetics (i.e. scaled in time). In other words, the time dependent properties, such as contact angle and viscosity would have the same evolution, but they are scaled with respect to the final time so that the time factor is calculated as $t_{scale} = t_{final}/16h$ (16 h was the time of the reference sol). Accordingly, the contact angle has been fitted by the following relation for any gelation time

$$\theta(t) = \theta_0 + 0.01277 \cdot t/t_{scale} - 17.133 \cdot e^{-0.55 \cdot t/t_{scale}} \quad (\text{for } t \le t_{final}) \tag{14}$$

And viscosity has a linear approximation with the coefficient as shown in Table 9.

For each pore size we performed 10,000 MC realizations. Fig. 8 presents an example for 1 μm pore size of scattered data graphs of these realizations. Similar results are produced for each pore size. From these graphs we can deduct that the impregnation treatment can penetrate between 1 cm as the minimum penetration depth to a maximum penetration depth of 8 cm for 1 μm pore size. Spearman's correlation parameters r_s are calculated from these results and give an information about the correlation between a parameter x_i and a penetration depth y.

Table 8
Parameter ranges used for MC sampling. Values marked with * are the initial values for the time variable properties.

Variable	Unit	Min	Max
Viscosity* (μ)	mPa•s	3	8
Contact angle* (θ_0)	°	30	80
Density (ρ)	kg/m³	800	1200
Surface tension (σ	N/m	0.01	0.08
Gelation time	H	16	200

Table 9
Viscosity fitting parameters with scaled time.

Time [h]	A	b	t0
t/t_{scale} < 3	4.53	0.281	0
3<t/t_{scale} < 13	3·4.53	0.384	3
13<t/t_{scale} < 16	3·4.53 + 12·0.384	1.723	12

The correlation parameters are calculated for a set of pore sizes and they are shown in Fig. 9. For all physical parameters they are relatively constant for smaller pores, until a pore size of 1 μm. For small pores it is visible that the most sensitive parameter is surface tension The driving force behind the movement is the pressure difference created at the liquid–air interface (as long as the contact angle with the solid is lower than 90° resulting in a concave meniscus), which is proportional to the liquid–air surface tension as seen in the Young-Laplace equation and inversely proportional to the radius (see Eq. (3)). Hence, surface tension is positively correlated with the penetration depth and results in higher suction force, if the liquid wets the material (larger penetration), as its value increases.

As well, time of gelation is an important positively correlated parameter assuring higher penetration if the kinetics of gelation are slower. As experimentally measured, the sol experiences a sudden change in their properties moments before gelation (when it behaves like a solid) which hinders or halts its movement through the pore structure.

On the contrary, higher contact angle results in lower penetration depth, which is also in line with the Young-Laplace equation. Density, on the other hand, have only negligible effect on the penetration depth. Surprisingly, the influence of viscosity was found to be barely significant. Although viscosity is typically considered the key factor for impregnation treatments penetration, it should be taken into account that the viscosity values considered for the study were in the typical range of the alkoxysilane-based sols and thus, this parameter would be expected to have a higher influence for very viscous liquids.

For larger pores the correlation parameters are different. The importance of surface tension increases with larger pore sizes, while the gelation time does not play an important role anymore.

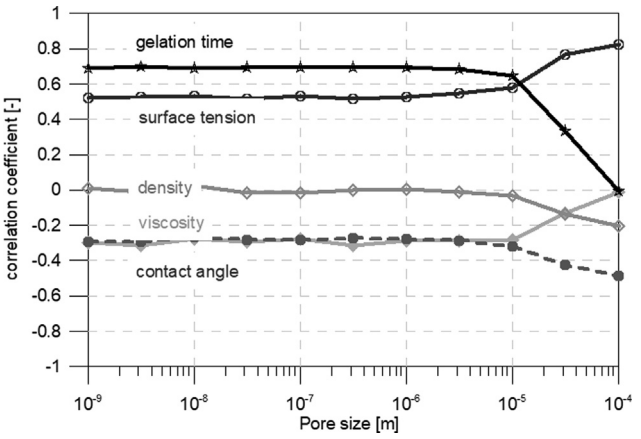

Fig. 9. Ranked correlation coefficients for sol physical properties and different pore sizes.

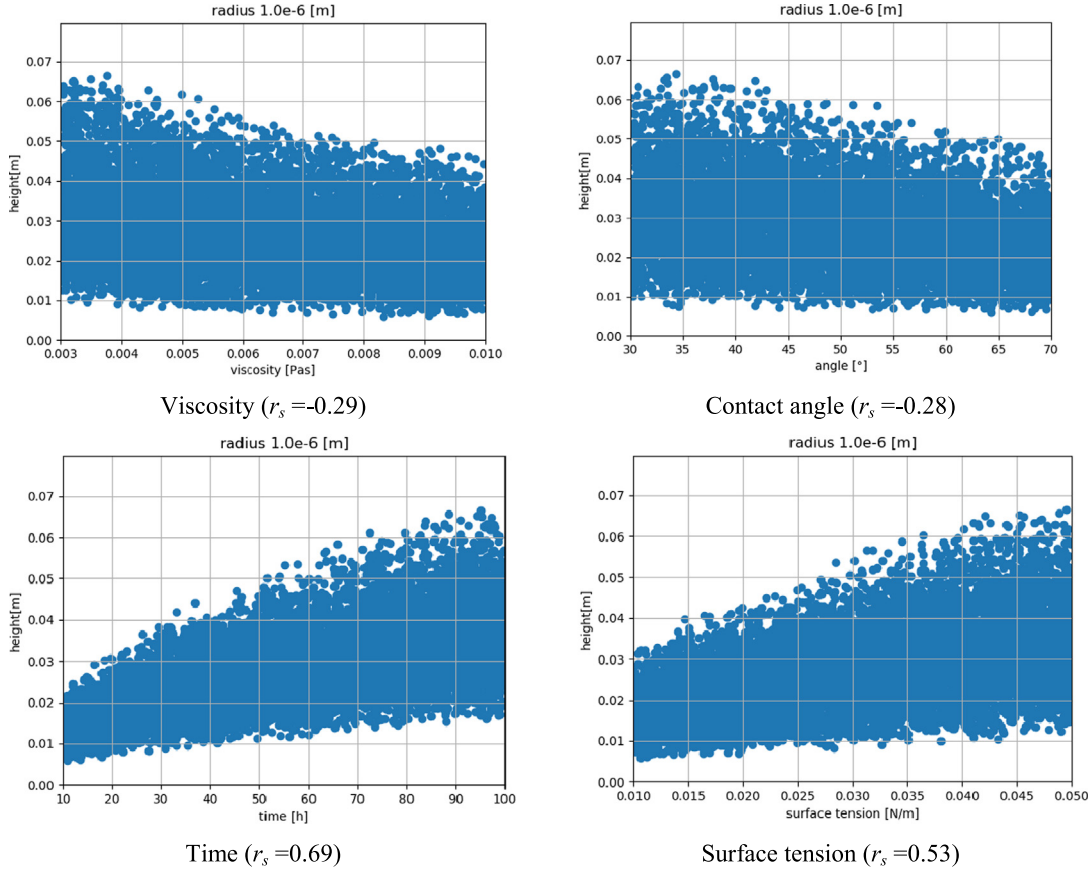

Fig. 8. Scatter plots for viscosity, contact angle, gelation time and surface tension for pore size 1 μm.

This is because the fluid quickly penetrates into larger pores before it has time to gel. Also in line with the influence of capillary forces, the importance of contact angle, which depends on the balance of surface free energies at the solid–liquid-air interface, slightly increases in anti-correlation, meaning that with larger pores lower contact angle gives higher penetration depth. The influence of viscosity becomes smaller for larger pore sizes because the viscous pressure loss is inversely related to the square of the radius, while the Laplace pressure (driving force) is only inversely proportional the radius.

5. Validation of the sensitivity study results

In contrast with the conventional consideration of viscosity as the most determining parameter for the penetration depth, the results in Fig. 9 suggest that the most important optimization parameters are the gelation time and surface tension. The rank of importance depends on the pore size. We tested these conclusions on a "s/c 3/1 w/c 0.5" sample, by comparing the penetration and uptake at ambient temperature (20 °C) and at lower temperature −10 °C, in order to modify the sol properties. Exact value of physical parameters at this temperature is not easy to measure, especially their time dependence, but we can expect changes in sol properties and their effect on the penetration depth as described in Table 10.

Viscosity increases with lower temperature. Because it is negatively correlated with the penetration depth its increase results in lower penetration depth. Contact angle will not change significantly [28] with temperature. Density will increase, but its effect will depend on the orientation of the application and the influence is small. Surface tension and gelation time will increase and both are predicted to result in higher penetration depth. Since the correlation of the latter two parameters is larger than the sensitivity to viscosity we expect increase of the penetration depth with lower temperature.

By cooling down the sample there is a possibility of water condensation from the ambient moisture that may alter the experimental results. Accordingly, the mortar was dried at 40° as the other ones and, after reaching ambient temperature, it was sealed in ziplock bags before being placed the freezer.

Gelation time has been experimentally determined to be 90 h. Surface tension was derived indirectly from the column wicking experiment where the capillary rise of the sol was observed in 1.15 mm diameter glass tubes at 20 °C and at −10 °C. The measured heights were 8 mm at 20 °C and 10.5 mm at −10 °C. According to Jurin's law (Eq. (15)) the height should be proportional to the surface tension (since the difference in contact angle and density are small). The surface tension calculated with this approach is 30 mN/m and viscosity increases from 4.6 cP at 20 °C to 5.6 cP at −10 °C.

$$h = \frac{2\sigma \cos\theta}{\rho g r} \tag{15}$$

Experimental results show that the penetration depth indeed increased from 2.0 mm (0.5 mm standard deviation) at 20 °C to 5.8 mm (3.6 mm standard deviation) at −10 °C. Accordingly, the uptake also increased from 225 g/m^2 at 20 °C to 925 g/m^2 at −10 °C. The values obtained numerically from the sol physical properties were 4.1 mm depth and 379 g/m^2 uptake at 20 °C and 7.1 mm depth and 744 g/m^2 uptake at −10 °C. As it can be seen, the trend for the numerical values is in good agreement with the experimental results, which additionally validates the developed model. However, some differences can be observed in the magnitude of the values which can be attributed to the difficulty of maintaining equal moisture levels at both temperatures (a factor that can affect gel time and penetration) and the assumptions made for the calculations, namely: (1) the variation of physical properties with time was assumed to follow the same trend regardless of temperature, (2) temperature remains constant during the whole experiment.

Table 10
Expected change of sol properties at lower temperature.

Variable	Property change [increase (+)/decrease(−)]	Penetration depth change [increase (+)/decrease(−)]
Viscosity* (μ)	+	–
Contact angle* (θ_0)	0	0
Density (ρ)	+	+/−
Surface tension (σ	+	+
Gelation time	+	+

6. Conclusions

The purpose of the presented analysis is to determine which sol's physical properties should be optimized for the given material in order to achieve maximal penetration depth. The analysis reveals that the influence of each property varies with the pore size following a different trend. This is especially true for pores >10 μm. For all pore sizes the most important parameters are gelation time and surface tension. While the importance of surface tension is positively correlated with the pore size, the opposite is true for the gelation time. The importance of contact angle and density slightly increase with larger pores, but their overall importance is lower. Hence, for the optimization process of the sol, it is required to know beforehand the pore size distribution of the material; a degraded material can have large pores and cracks and sound material have larger amount of smaller pores. Based on these results the sol components should be mixed in a way to increase surface tension and gelation time. This has been demonstrated by the results of the cooled sample, where the penetration depth more than doubled if the experiment has been performed at −10 °C compared to 20 °C. In other words, the impregnation products have better penetration depth when applied at lower temperatures. It should be noted that other parameters, such as aesthetic indicators and cracking potential, are not taken into consideration at this step and should be considered in later optimization stages.

In terms of modelling conclusions, it is obvious that the theoretical model does not represent well the properties of cementitious materials and largely overestimates the penetration depths. The results demonstrate that the viscous pressure drop in pores can be significantly higher than theoretically given. This feature should be considered in a cases where the assumption of a cubic law (Hagen-Poiseuille flow) is taken forward, e.g. pore-network models [16], fracture flow,... It can also have consequences for the pore-scale models [28,29] where the roughness along the pores cannot be explicitly represented. This is in-line with earlier observations for fractured rocks e.g. [30] where the three conditions to apply the cubic law are given as (1) sufficient length of a pore, (2) low surface roughness and (3) limited inertial effects (low Re). The first criterion is not valid as demonstrated from the optimization calculations in Eq. (13). Most pores are just slightly prolonged, with the single exception of micro-fractures. The second criterion also do not apply to cementitious materials as it is known that the microstructure is very heterogeneous on small scales. So the pore roughness is large relative to the pore size. This is more pronounced for smaller pores.

The next step in the optimization process is to find the optimal mixture of sol constituents to assure the best penetration depth and hence durability of surface treatments.

7. Data availability

The raw and processed data required to reproduce these findings are available to download from https://data.mendeley.com/datasets/publish-confirmation/4fvzs8b3md/1

CRediT authorship contribution statement

Janez Perko: Conceptualization, Methodology, Formal analysis, Software, Writing - original draft, Writing - review & editing, Visualization. **Rafael Zarzuela:** Conceptualization, Methodology, Validation, Investigation, Writing - original draft, Writing - review & editing. **Inés Garcia-Lodeiro:** Validation, Resources, Writing - original draft, Writing - review & editing. **María Teresa Blanco-Varela:** Resources, Supervision, Writing - review & editing. **Maria J. Mosquera:** Writing - original draft, Writing - review & editing, Funding acquisition, Project administration. **Timo Seemann:** Methodology. **Li Yu:** Methodology, Software.

Declaration of Competing Interest

The authors declare that they have no known competing financial interests or personal relationships that could have appeared to influence the work reported in this paper.

Acknowledgements

The work described in this manuscript has been performed under InnovaConcrete EC project, supported by funding from the European Union's Horizon 2020 Research and Innovation Programme under Grant Agreement N° 760858.

References

[1] F. Stangenberg, R. Breitenbücher, O.T. Bruhns, D. Hartmann, R. Höffer, D. Kuhl, G. Meschke, Lifetime-oriented Structural Design Concepts, Springer, Berlin Heidelberg, Berlin, Heidelberg, 2009.
[2] Q.T. Phung, N. Maes, D. Jacques, J. Perko, G. De Schutter, G. Ye, Modelling the evolution of microstructure and transport properties of cement pastes under conditions of accelerated leaching, Constr. Build. Mater. 115 (2016) 179–192.
[3] V.H. Nguyen, B. Nedjar, J.M. Torrenti, Chemo-mechanical coupling behaviour of leached concrete, Nucl. Eng. Des. 237 (20–21) (2007) 2090–2097.
[4] X. Pan, Z. Shi, C. Shi, T.-C. Ling, N. Li, A review on concrete surface treatment Part I: types and mechanisms, Constr. Build. Mater. 132 (2017) 578–590.
[5] A. Custance-Baker, S. Macdonald, Conserving Concrete Heritage Experts Meeting, The Getty Conservation Institute, Los Angeles, California, 2014.
[6] G. Wheeler, Alkoxysilanes and the Consolidation of Stone, The Getty Conservation Institute, Los Angeles, California, 2005.
[7] A. Barberena-Fernández, P. Carmona-Quiroga, M. Blanco-Varela, Interaction of TEOS with cementitious materials: chemical and physical effects, Cem. Concr. Compos. 55 (2015) 145–152.
[8] F. Sandrolini, E. Franzoni, B. Pigino, Ethyl silicate for surface treatment of concrete – Part I: pozzolanic effect of ethyl silicate, Cem. Concr. Compos. 34 (3) (2012) 306–312.
[9] R. Zarzuela, M. Luna, L. Carrascosa, M. Yeste, I. Garcia-Lodeiro, M. Blanco-Varela, M. Cauqui, J. Rodríguez-Izquierdo, M. Mosquera, Producing C-S-H gel by reaction between silica oligomers and portlandite: a promising approach to repair cementitious materials, Cem. Concr. Res. 130 (2020) 106008.
[10] M. Bofeldt, B. Nyman, Penetration depth of hydrophobic impregnating agents for concrete / Eindringtiefe von Hydrophobierungsmitteln in Beton, Restoration Build. Monuments 8 (2–3) (2014) 217–232.
[11] C.J. Brinker, G.W. Scherer, Sol-Gel Science: The Physics and Chemistry of Sol-Gel Processing Presents the Physical and Chemical Principles of the Sol-Gel Process, Academic Press Inc, San Diego, California, 1990.
[12] M. Medeiros, P. Helene, Efficacy of surface hydrophobic agents in reducing water and chloride ion penetration in concrete, Mater. Struct. 41 (2008) 59–71.
[13] A. Johansson, M. Janz, J. Silfwerbrand, J. Trägårdh, Penetration depth for water repellent agents in concrete as a function of humidity porosity and time, J. Restoration Build. Monuments 13 (1) (2006) 3–16.
[14] A. Fakhari, T. Mitchell, C. Leonardi, D. Bolster, Improved locality of the phase-field lattice-Boltzmann model for immiscible fluids at high density ratios, Phys. Rev. E 96 (2017) 053301.
[15] Y. Zu, S. He, Phase-field-based lattice Boltzmann model for incompressible binary fluid systems with density and viscosity contrasts, Phys. Rev. E 87 (2016) 043301.
[16] Qingrong Xiong, Todor G. Baychev, Andrey P. Jivkov, Review of pore network modelling of porous media: Experimental characterisations, network constructions and applications to reactive transport, J. Contam. Hydrol. 192 (2016) 101–117, https://doi.org/10.1016/j.jconhyd.2016.07.002.
[17] E. Washburn, The dynamics of capillary flow, Phys. Rev. 18 (1921) 273–283.
[18] C. Weber, H. Stanjek, Development of diffuse double layers in column-wicking experiments: implications for pH-dependent contact angles on quartz, J. Colloid Interface Sci. 387 (2012) 270–274.
[19] Q.T. Phung, N. Maes, D. Jacques, Application of multiple techniques to quantify pore structure of degraded cementitious materials, in: XIV DBMC 14th International Conference on Durability of Building Materials and Components, Ghent, 2017.
[20] J.F. Illescas, M.J. Mosquera, Producing surfactant-synthesized nanomaterials in situ on a building substrate, without volatile organic compounds, ACS Appl. Mater. Interfaces 4 (8) (2012) 4259–4269.
[21] R. Wenzel, Resistance of solid surfaces to wetting by water, J. Ind. Eng. Chem. 28 (1936) 988–994.
[22] J. Bezanson, A. Edelman, S. Karpinski, V.B. Shah, Julia: a fresh approach to numerical computing, SIAM Rev. 59 (1) (2017) 65–98.
[23] S. Babaei, S. Seetharam, U. Muehlich, A. Dizier, G. Steenackers, B. Craeye, A multiscale framework to estimate water sorption isotherms for OPC-based materials, Cem. Concr. Compos. 105 (2020) 103415.
[24] C.S. Seetharam, A.R. Patel, J. Perko, D. Jacques, Quantification of leaching kinetics in OPC mortars via a mesoscale model, Constr. Build. Mater. 180 (2018) 614–628.
[25] A. Leemann, R. Loser, B. Münch, Influence of cement type on ITZ porosity and chloride resistance of self-compacting concrete, Cem. Concr. Compos. 32 (2010) 116–120.
[26] M. Simeone, I.B. Hogue, C.J. Ray, D.E. Kirschner, A methodology for performing global uncertainty and sensitivity analysis in systems biology, J. Theor. Biol. 254 (1) (2008) 178–196.
[27] M.C. Phillips, A.C. Riddiford, Temperature dependence of contact angles, Nature 205 (4975) (1965) 1005–1006, https://doi.org/10.1038/2051005b0.
[28] M. Zalzale, P. McDonald, K. Scrivener, A 3D lattice Boltzmann effective media study: understanding the role of C-S-H and water saturation on the permeability of cement paste, Modelling Simul. Mater. Sci. Eng. 21 (2013) 085016.
[29] M. Zhang, G. Ye, K. van Breugel, Microstructure-based modeling of permeability of cementitious materials using multiple-relaxation-time lattice Boltzmann method, Comput. Mater. Sci. 68 (2013) 142–151.
[30] A.P. Oron, B. Berkowitz, Flow in rock fractures: the local cubic law assumption reexamined, Water Resour. Res. 34 (11) (1998) 2811–2825.
[31] P. Maravelaki-Kalaitzaki, N. Kallithrakas-Kontos, D. Korakaki, Z. Agioutantis, S. Maurigiannakis, Evaluation of silicon-based strengthening agents on porous limestones, Prog. Org. Coat. 57 (2006) 140–148.
[32] A. Fakhari, M. Rahimian, Phase-field modelling by the method of lattice Boltzmann equations, Phys. Rev. E 81 (2010) 036707.
[33] M.J. Mosquera, D.M. de los Santos, A. Montes, L. Valdez-Castro, New nanomaterials for consolidating stone, Langmuir 24 (6) (2008) 2772–2778.
[34] Andreas Momber W, The wettability of some concrete powders, Particulate Science and Technology 20 (3) (2002) 243–246, https://doi.org/10.1080/02726350216092.